RESEARCH ARTICLE

Editor's Choice

**ADVANCED
ENGINEERING
MATERIALS**

www.aem-journal.com

Mixed Oxide Aerogels with High-Performance Insulating Properties for High-Temperature Space Application

Markus Heyer, Burkard Esser, Ali Guelhan, Barbara Milow, and Pascal Voepel*

Herein, a direct comparison of the thermal conductivity and stability of different silica-fiber-reinforced silica aerogels is presented. The thermal performance under high-temperature exposure within an arc-heated facility is evaluated by means of thermal propagation and stability. All aerogel materials, tested within this study, outperform the high-temperature fiber-based insulation mat in terms of thermal protection. Modification of the aerogels in the composition and opacification leads to an improvement of thermal insulation properties as well as of thermal stability against the high temperature. All materials are prepared in the form of cylindrical disks of 100 mm diameter having a thickness of 20 mm. Based on classic silica aerogel, an opacified silica aerogel and an aerogel in mullite composition, inorganic fiber-reinforce composites have been prepared and tested, and their performance is discussed comparatively. The specimens with mullite composition are intended to form mullite in situ during application to avoid energy-costly pretreatment.

1. Introduction

Metal oxides, especially mixed metal oxides are typically chosen for high-temperature applications, for example, as slurries for oxidic ceramic matrix composites.[1] The majority of these materials are alumina or zirconia based, or composed of mixtures of these materials with other oxides, mixed oxides such as mullite or dopant-stabilized oxides.[1,2]

Unlocking this potential of metal oxides within the material spectrum of aerogels would further boost their applicability in the high-temperature environments. Aerogels are open porous

M. Heyer, B. Milow, P. Voepel
Institute of Materials Research
German Aerospace Center
Linder Hoehe, 51147 Cologne, Germany
E-mail: pascal.voepel@dlr.de

B. Esser, A. Guelhan
Institute of Aerodynamics and Flow Technology
German Aerospace Center
Linder Hoehe, 51147 Cologne, Germany

B. Milow
Department of Chemistry
Nanostructured Cellular Materials
Greinstraße 6, 50939 Cologne, Germany

The ORCID identification number(s) for the author(s) of this article can be found under https://doi.org/10.1002/adem.202300625.

materials prepared via a sol–gel process in combination with a controlled drying process, e.g., supercritical drying, freeze drying, which prevents the collapse of the pores while extracting the solvent.[3] The first aerogel ever was produced by Kistler in the early 1930s.[4] In his article, he described the importance of a controlled drying process for the shrinkage-free drying of the "jellies". However, these materials were not significantly further investigated due to the emergence of polymers. Over the past few decades, aerogels have become prominent for their application as high-performance materials in diverse research fields. Besides different emerging fields of application such as filtering,[5] energy storage and conversion,[6] and acoustic insulation,[7] the industrialization of aerogels is seeing a rapid growth. The thermal protection still remains one of the most prominent applications of aerogels. Besides the super-insulating performance, other characteristics of aerogels such as those mentioned previously have not yet been applied at an industrial scale.

One of the most well-studied aerogels is the inorganic SiO_2 aerogels. The material parameters such as thermal conductivity, shrinkage, mechanical behavior, and the effect of supercritical drying have been investigated in several papers. These aerogels are famous for their very low thermal conductivity (around $15\,mW\,m^{-1}K^{-1}$), but they are prone to sintering at temperatures at or over 400 °C.[8]

Aerogels that are more stable to higher temperatures can, for example, be produced from the elements Zr,[9] Ti,[10] Al,[2b,11] Si,[8] Yr,[12] and Ba[11b,13] as oxides in pure form or as hybrids. The main challenges to synthesize these special aerogel types are the chemical costs, increased chemical synthesis activities, and the toxicity of the reactants for the chemical reactions, as well as the lengthy washing process for salt-based reactants.[11a,14]

The interest in aerogels, however, remains high as can be illustrated by the latest calls from the European Union for aerogel materials[15] or the announcement from the IUPAC.[16] Some of the most prominent high-temperature-resistant aerogels in literature are based on alumina[17] or zirconia.[18] Since single-component aerogels often lack performance for long-term high-temperature applications in terms of shrinkage or thermal stability, metal oxide composite aerogels have been developed which are mostly based on one of the well-established single-component aerogels such as silica-stabilized alumina[19] or zirconia-based alumina aerogels.[20]

**ADVANCED
SCIENCE NEWS**

www.advancedsciencenews.com

**ADVANCED
ENGINEERING
MATERIALS**

www.aem-journal.com

Recently, we presented different syntheses approaches for fiber-reinforced opacified oxidic aerogel materials and their high potential as thermal protection shielding.[21] These aerogel materials were optimized with respect to the shrinkage behavior and thermal conductivity at room temperature.[21] While these results were promising for room-temperature applications, high-temperature applications demand analytical techniques that are scarce and thus reported rarely in the literature.

In general, different factors such as weight, manufacturing costs, processing environmental compatibility/reusability, and durability have to be considered for technical insulation application areas such as, e.g., in aeronautics and aerospace.

In spaceflight operations typically, thermal protective systems (TPS) are considered for protection of severe kinetic heating and thermal protection in terms of interaction with flames with sensitive parts during launch or re-entry and the protection of the fairing or that of satellites. These TPS are needed to protect the structural parts of the spacecraft from damage.

In general, TPS can be categorized into three systems: passive, semi-passive, and active, as depicted in **Figure 1**.

In 1957, the first approach to develop TPS using resin-filled fibers was presented, which had been formed under heat to carbonaceous mass, which adsorbed six times more heat than boiling water.[22]

Since then, numerous materials have been developed based on the physical principle of ablation, they can only be used once since the protection mechanism is based on the sacrificial degradation of the protective material. So, the limiting factor is the heat resistance of the material.[22–24] It has been demonstrated that cork as a natural material could serve as an energy absorption material and could be combined with C/C-SiC reinforced carbon–carbon (RCC) and carbon/epoxy backup.[25] In general, these materials are considered as ablative TPS. The material itself decomposes upon thermal impact and releases gaseous products. These gasses protect the structure from heat fluxes.

One famous example is phenolic impregnated carbon ablator (PICA), which originally was developed by NASA in the 1980s for the heat shield of the Stardust Return Capsule.[26] The reentry of this capsule was roughly 120 s with respect to the transition and continuum until the Drogue chute was deployed.[27] Other organic, aromatic, phenolic resin-impregnated fibers had also been developed until the 1980s.[28] PICA was further optimized by SpaceX and named PICA-X and considered for application within the Dragon Spacecraft as well as for the Falcon 9 second Stage.[29] Another TPS material is represented by so-called super-lightweight ablators (SLV)[30] having been investigated within the Mars 2020 project of NASA for the MEDLI2 mission (Mars Entry, Descent, and Landing Instrumentation 2) on be

backshell of the capsule.[31] The other possibility is to reuse the TPS tiles for several missions. In this case, the heat protection must not depend on thermal degradation of a sacrificial ablator.[32] The method of active cooling removes the accumulated heat from the heat shield and structure through a medium, such as gas.[33] Also, the evaporation enthalpy by, e.g., liquid methane which is conducted through the heat shield and evaporates on the hot side through a series of dots can be used.[34] However, the need of highly efficient and super lightweight TPS materials still remains.

2. Results and Discussion

Based on an early synthesis protocol by Hurwitz et al.[11a] the optimized fiber-reinforced aerogel in mullite composition was developed. The focus of our protocols was the reduction of hazardous propylene oxide. This could be reduced from $AlCl_3$:PO with 1:8 to 1:3.75 and afterward the sol was impregnated within a fiber mat.

In the first approach, the synthesis routine was optimized to produce aerogel specimens with low shrinkage and to avoid cracking. With this optimization, the production of composite parts for thermal shielding was realized. Initially, the amount of propylene oxide was drastically reduced in comparison to the literature to minimize the health risks.[11a] Subsequently, the solvent amount was tuned to result in stable monolithic aerogels.

Figure 2 depicts the optical appearances of representative specimens with a diameter of ≈50 mm. Clearly, the solvent adjustment led to an optical densification of the aerogel and the formation of mechanically more stable monoliths. The adjustment of the solvent has shown that a decrease in the overall solvent amount enables the mentioned formation. However, the ratio of ethanol and water remained constant (5:16).

Subsequently, the aerogels have been prepared as fiber-reinforced composites and compared to already described approaches[21] in performance in an arc-heated facility. **Figure 3** depicts a representative aerogel composite specimen placed into the arc-heated facility. For analysis, the specimens were kept inside of the stream for 120 s and then extracted. The specimens were evaluated subject to their optical appearance and their integrity before and after this thermal treatment.

Figure 4 summarizes the optical changes of the four different investigated specimens upon high-temperature impact in temporal evolution within this comparison. Although the glass fibers are stated to show a classification temperature of 1,200 °C, the usage of the fibers should be limited to 1,100 °C according to the manufacturer. Also, the chemical composition of the fibers is stated to be SiO_2 (61–67 wt%), CaO (27–33 wt%), MgO
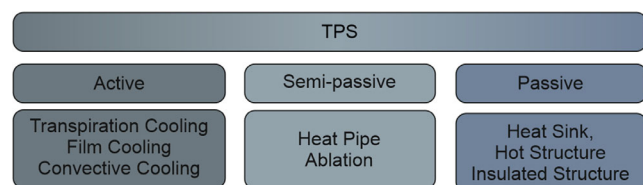

Figure 1. Different types of TPS. Adapted with permission.[23] Copyright 2020, Elsevier. In this article, the focus is on passive/semipassive insulation materials as TPS protection material.
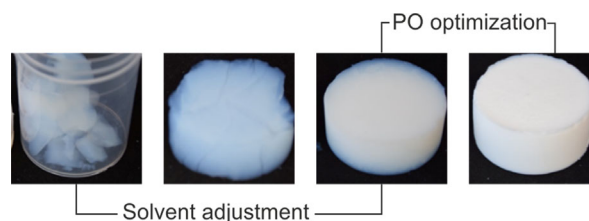
Figure 2. Schematic depiction of the macroscopic appearance of the aerogels based on solvent and PO adjustment/optimization.

Figure 3. Representative photograph of an aerogel composite specimen (mullite composition) entering the arc-heated facility.
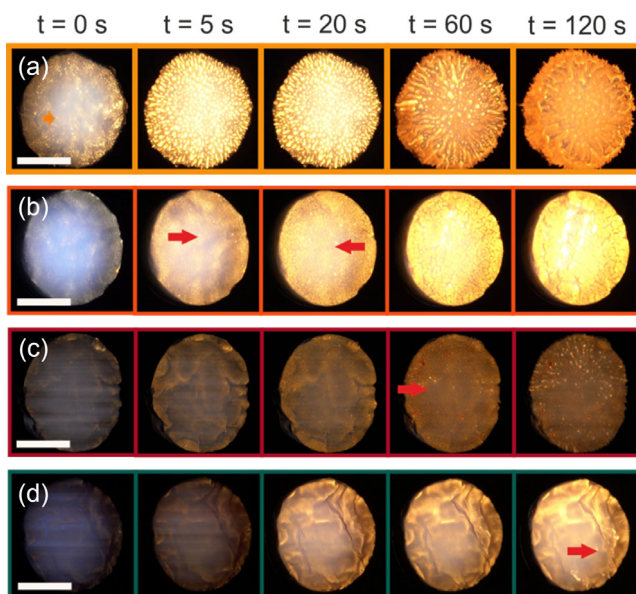
Figure 4. Temporal evolution of the surface of the investigated samples during the exposure to high temperature over a period of 120 s. Pristine fiber mat a), fiber-reinforced silica aerogel b), opacified fiber-reinforced silica aerogel c), and fiber-reinforced aerogel with mullite composition d). All scale bars are 50 mm.

(2.5–6.5 wt%), and traces of Al_2O_3 (<1 wt%) and Fe_2O_3 (<0.6 wt%).[35] It can clearly be observed that the fibers begin to melt within seconds after exposure to high temperatures. Also, erosion can be observed. The integrity of the fiber mat is no longer preserved, and the melted glass is transported toward the outer regions of the specimen, thus indicating the effect of high temperature. Direct measurement of the surface temperature is not trivial because of the porous and white surface. The melting of the fibers indicates that temperatures of far more than 1,200 °C were reached immediately in the experiments. Typically, a material with the given compositions (neglecting aluminum and iron contents) of the fibers exhibits a melting point of ≈1,400 °C.[36] A schematic phase diagram is depicted in Figure S1, Supporting Information.

This behavior changes with the addition of aerogel. After exposure to the high temperature, the surface of the aerogel specimen starts to glow as well but melting does not occur. The fibers are protected by the aerogel. This is further improved by the addition of an opacifier (boehmite) and the phase transition to the mullite system. Comparing the photographs after 120 s of high-temperature exposure it can be seen that the material transport in terms of melted glass is reduced by further improving the aerogel system. In the case of the mullite aerogel, only very few droplets can be seen on the surface which might be attributable to fibers that are not covered by the aerogel. Also, the time after which these droplets form is delayed by the modification of the materials. For the pristine fiber mat, the drops of molten matter are already visible in the first frame after exposure to the high temperature. In the case of the silica aerogel with fiber reinforcement, these droplets appear to form between 5 and 20 s. The addition of boehmite as opacifiers further delays this formation to ≈60 s. This could be due to single pure silica aerogel regions present that were not crosslinked with boehmite. And in the case of the mullite material individual droplets are only visible after the full period of 120 s (note: *exemplarily indicated by arrows in the respective frame*). In the case of the mullite composition, it can be observed that details of the surface contour of the sample remain unchanged which is clearly not the case for the other samples depicted, indicating the improved thermal stability of this very system.

Figure 5a depicts the optical appearance of the different specimens before and after the exposure to the high temperature for 120 s. As described previously, the pristine glass fibers show strong degradation due to the high-temperature exposure. The pristine glass fiber mat begins to melt at 1,330 °C.[37] The material is molten and dragged toward the outer regions of the specimen.

The thickness is drastically reduced as the formerly airy "cotton candy"-like structure is destroyed completely. The surface appears yellow/brownish and partially crystalline. The addition of silica aerogel (Figure 5b) improved the performance of the material but the comparison of the specimen before and after high-temperature treatment reveals drastic changes in the surfaces due to sintering. Also, delamination of the sintered regions from the remaining sample can be observed (*indicated in Figure 5b by a red-colored arrow*). However, the sample does not show such drastic degradation as the pristine fibers. Also, the aforementioned color change is not observed. The surface also seems to be partially crystallized. These crystals break off and cause the detachments of the very first surface layers.

The addition of an opacifier as depicted in Figure 5c seems to prevent the delamination. As we have already demonstrated the addition of boehmite into the silica aerogel fiber composite has a beneficial influence on the mechanical behavior.[21] This improvement prevents the sample from delamination. The surface however also suffers from heavy sintering and crystallization effect. Nevertheless, the integrity is not destroyed and the thermal protection function of the material is preserved for longer mission times.

The optical inspection of the sample based on fiber-reinforced mullite aerogel confirms the results stated above. The surface remains intact. Only slight sintering can be observed. The amount of crystallization and sintering is drastically decreased. The complete integrity of the surface remains intact.

SEM micrographs have been recorded to investigate the structural changes in the specimens during the high-temperature exposure. As already indicated in Figure 5 the fiber specimen's
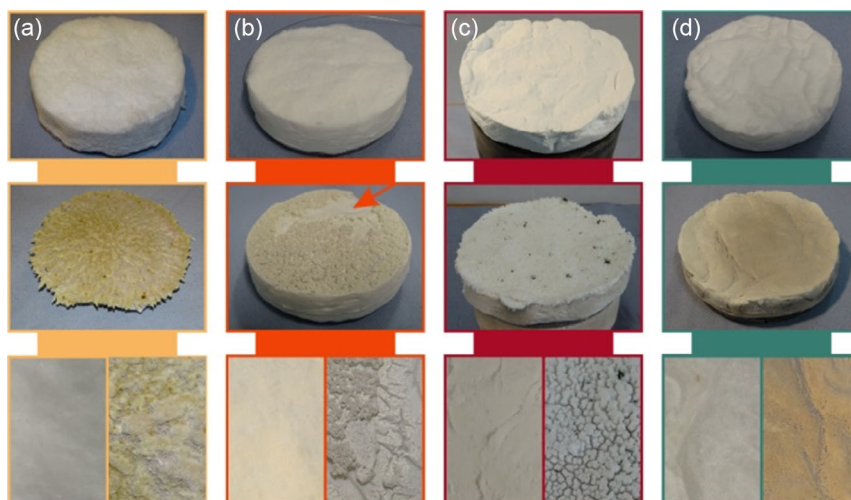
Figure 5. Photographs of the different samples prior to and post high-temperature exposure for 120 s. Pristine fiber mat a), fiber-reinforced silica aerogel b), opacified fiber-reinforced silica aerogel c), and fiber-reinforced aerogel with mullite composition d).
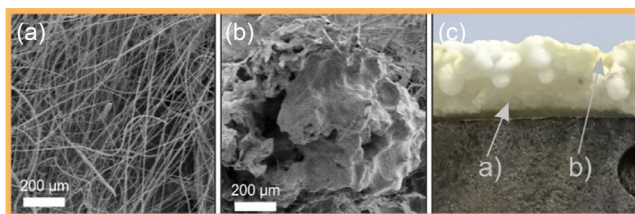
Figure 6. SEM micrographs of the pristine fibers used in the experiment at the bottom a) and the top b) of the high-temperature exposed specimen, representative location for the sample preparation c).

Figure 7. SEM micrographs of the fiber-reinforced aerogel used in the experiment at the bottom a) and the top b) of the high-temperature exposed specimen, representative location for the sample preparation c).
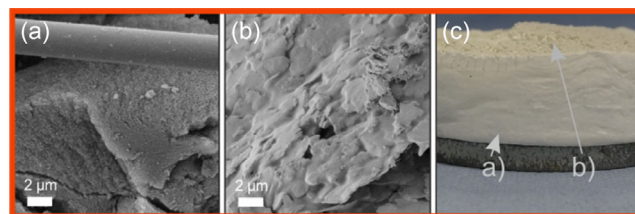
integrity was totally destroyed during the exposure to the high temperature. In **Figure 6**, scanning electron micrographs are shown at two different locations of the pristine fiber sample after the high-temperature exposure. Figure 6a represents a spot at the very bottom of the sample and exhibits the structure of the fiber mat. The fiber structure is clearly visible. Figure 6b shows the sample at the very top of the specimen after high-temperature exposure. The fiber structure is no longer visible. Melting and heavy sintering effects have taken place although the designed maximum application temperature does not seem to be reached during the experiments.[35]

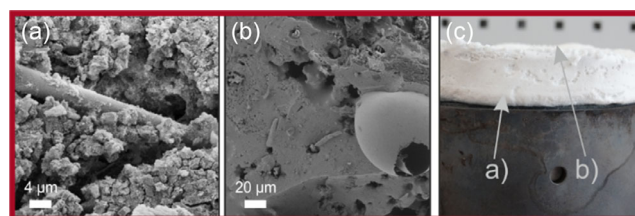**Figure 7** depicts the respective locations of the fiber-reinforced aerogel sample.

As shown in Figure 7a, the aerogel structure as well as the fibers remain intact at the bottom of the specimen. In contrast, the top surface layer is completely molten and covered with dense matter. The pure aerogel itself does not seem to be able to withstand the high temperatures and conditions provided by the applied high temperature.

Figure 8 depicts representative SEM micrographs of the opacified specimen. As expected, Figure 8a shows the similar structure of the pristine composite as previously reported.[21] All three components are visible in the composite.

The fibers and cuboidal boehmite particles are surrounded by the silica aerogel matrix.

Figure 8. SEM micrographs of the opacified fiber-reinforced aerogel used in the experiment at the bottom a) and the top b) of the high-temperature exposed specimen, representative location for the sample preparation c).

In Figure 8b, the upper side of the specimen is depicted. As for the other samples, some molten areas are visible which are attributable to the fibers melting in the high temperature. As already indicated above, sintering and crystallization occur on the top side of the sample. In contrast to the other samples, this sample is the only one exhibiting bubble structures on the surface hinting toward a gas evolution in the melt (*for more SEM micrographs please check ESI* Figure S2, Supporting Information).

Figure 9 depicts the respective SEM micrographs of the fiber-reinforced aerogel sample with mullite composition. As for the other cases, Figure 9a depicts a representative location in the bottom region of the sample. In the top region of the picture, a fiber
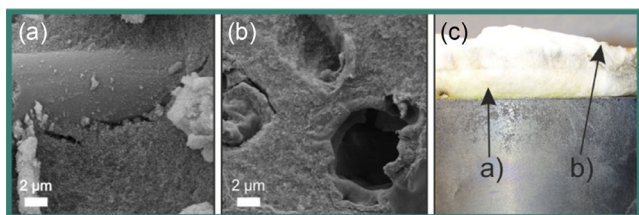
Figure 9. SEM micrographs of the fiber-reinforced aerogel with mullite composition used in the experiment at the bottom a) and the top b) of the high-temperature exposed specimen, representative location for the sample preparation c).

of the Insulfrax is visible. It is surrounded by an aerogel matrix. Due to possible mechanical stresses, the matrix seems to be detached from the fiber at the bottom side. The porous aerogel structure is also visible in the SEM image. Figure 9b depicts the upper side of the specimen. The porous structure is still present. However, larger holes are now present inside the material. These holes exhibit an approximate diameter as that of the former fibers. Also, the inner walls of these holes seem to be covered.

Based on the results indicated above, this cover might be based on molten fiber material. The fibers seem to melt upon high-temperature exposure as already indicated in Figure 6. This molten material lines the inner walls of the aerogel leaving holes inside the matrix.

Figure 10 depicts the diffraction patterns of each specimen on either side after exposure to high temperature. The lower diffraction pattern was recorded on the bottom side of each sample.

An exponential decay background subtraction was performed for all diffraction patterns. During the high-temperature exposure, all samples undergo drastic changes.

Figure 10a depicts the diffraction patterns of the pristine fiber mat. No crystalline components are detectable within the fiber mats on the bottom side (cf. Figure 10a). However, these changes are due to the direct exposure to the high temperature. Distinct peaks appear within the pattern. Based on the given composition of the fiber mats SiO_2 (61–67 wt%), CaO (27–33 wt%), MgO (2.5–6.5 wt%), and traces of Al_2O_3 (<1 wt%) and Fe_2O_3 (<0.6 wt%) different calcium and/or magnesium silicates are likely to form. The most prominent peaks can be attributed to cristobalite (PDF 82-1403) and are based on the high silica content of the fibers. Additionally, peaks at 26°, 27.7°, and 31.9° as well as 45.5° and 46.1° 2Theta hint toward calcium silicate (PDF 02-0506) and/or quartz (PDF 85-0795). Calcium silicates with heteroatoms, such as ferrobustamite (PDF 76-0900; $Ca_{0.82}Fe_{0.18}SiO_3$), wollastonite-1A (PDF 27-1056; $(Ca,Fe)SiO_3$) or diopside (PDF 82-0599; $CaMg(SiO_6)$), or Hedenbergite magnesian (PDF 74-2425; $Ca_{0.79}Al_{0.06}Fe_{0.08}Mg_{0.47}Fe_{0.6}Si_2O_6$) can also be identified.

Figure 10b depicts the diffraction patterns of the fiber-reinforced silica aerogel on the upper surface and the bottom area of the specimen, respectively. As indicated in Figure 10, the most prominent peak can be attributed to cristobalite (101). This observation is in full accordance with the fact that the absolute amount of silica species is increased in the total system, therefore, decreasing the manganese and or calcium impurities that come from reinforcement fibers. Species such
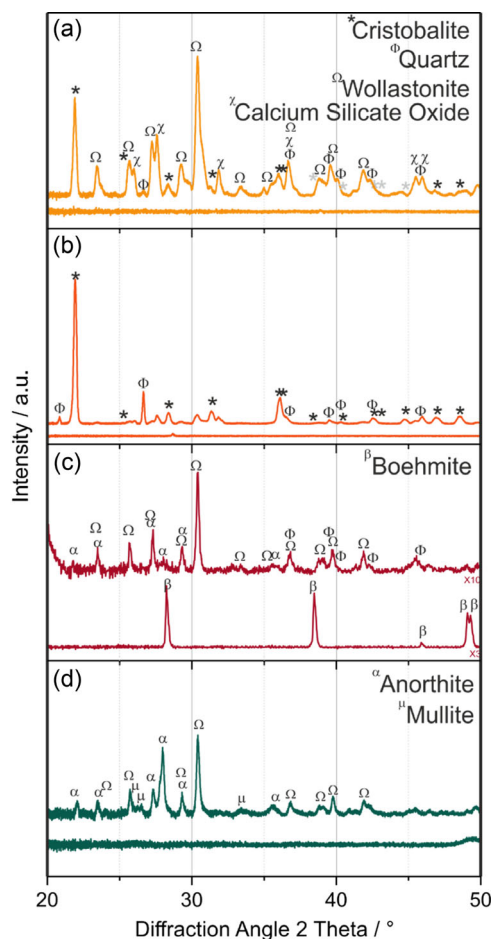
Figure 10. XRD patterns of pristine fiber mat a), fiber-reinforced silica aerogel b), opacified fiber-reinforced silica aerogel c), and fiber-reinforced aerogel with desired mullite composition d). The lower pattern represents the sample at the bottom of the specimen, and the upper pattern represents the sample from the top of the specimen after high-temperature exposure, respectively.

as calcium silicates oxides or mixed metal silicates become minority species in the specimen.

Figure 10c represents the diffraction patterns of the fiber-reinforced, opacified (boehmite) silica aerogels. In contrast to Figure 10a,b the diffraction pattern of the bottom side of the specimen does show distinct reflection maxima which can be assigned to boehmite crystals dispersed inside the specimen (indicated by "β"). The surface of the specimen which was exposed to the high temperatures does not exhibit any or only low signals of boehmite but significant diffraction maxima for sodium aluminum silicates. These findings in contrast to the above mentioned are based on the local increase of heteroatoms due to the incorporation of boehmite.

Figure 10d shows the diffraction patterns of the fiber-reinforced aerogel with mullite composition. The intrinsic thermal stability of the mullite system should exceed the performance of the other systems (cf. Figure S3, Supporting Information). The bottom diffraction pattern of the mullite system does not exhibit any diffraction peaks just as

**ADVANCED
SCIENCE NEWS**

www.advancedsciencenews.com

**ADVANCED
ENGINEERING
MATERIALS**

www.aem-journal.com

Figure 10a,b since no crystalline opacifier has been added to the material as it is done in Figure 10c. Based on the fiber mat (cf. Figure 10a), some peaks can be attributed to the melting and crystallization of the fiber materials. Unfortunately, mullite does not become the predominant modification within the sample which might be attributed to the short heating period of 120 s in the experiments. As one main modification anorthite (PDF 41-1486) can be assigned to the majority of the diffraction peaks. However, the thermal stability of the specimen is outstanding. As already discussed above, the high-temperature impact seemed to melt the fiber reinforcement on the top layers of the specimen. Based on the given composition of the fibers, this means that calcium will be incorporated into the system. If a ternary phase diagram (CaO-Al_2O_3-SiO_2) is regarded,[38] (see Figure S1, Supporting Information) an increase of calcium fraction for an otherwise mullite system would directly lead to the anorthite phase region and inhibit the mullite crystallization. This might explain the presence of anorthite in the specimen after thermal impact and melting of the fiber reinforcements. The influence of heteroatoms within mullite formation has already been demonstrated in literature.[39]

Additional Raman studies confirm the presence of anorthite within the sample (cf. Figure S4, Supporting Information, ESI). Also, Raman modes of mullite can be found in the spectrum. Especially, signals in the region of ≈275 and $400\,cm^{-1}$ hint toward the mullite formation since the reference spectrum of anorthite does not show these features.[40]

Based on additional ex situ experiments with longer aging times at elevated temperatures for 24 h, the formation of mullite can be seen for an aerogel by XRD analyses. This proves the possibility of phase formation of mullite within the aerogel sample (cf. **Figure 11**).

Also, the aerogel structure is preserved during the phase formation (Figure S5, Supporting Information). This fact shows that an energy-intensive process can be avoided and the aerogel could be transferred into the desired modification in situ. As already
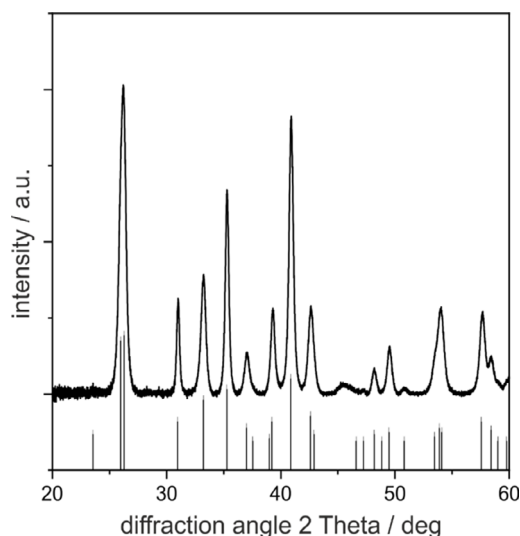
indicated by the optical photographs the measured temperature of the pristine fiber mat immediately melts under the high-temperature impact and therefore the temperature at the back-side of the specimen increases sharply (see **Figure 12**). Within the 120 s of exposure, the measured temperature of the backside of the sample increases drastically to almost 160 °C. The increase is only stopped by the fact that the sample was removed from the high temperature after 120 s. Although stated to be high-temperature stable, the fiber mat fails in our test setup indicating the high thermal impact of the high temperature on the test specimens.

All aerogel samples exhibit a comparably high thermal protection capability with temperature increases of ≈10–15 °C after 120 s and a total increase of ≈20–40 °C. Based on these investigations, the mullite-composition type aerogels exhibit superior performances compared to the other aerogel samples as the thermal degradation does not occur as prominent as for the pure silica-based aerogels. The initial temperature increase is slightly higher for the mullite composition which might be attributable to the fact that the mullite has to be formed in situ. However, the long-term performance of this very sample outperforms the other aerogel sample. The temperature increase after the high-temperature exposure is not as prominent as for the other samples. As it can be observed in Figure 4 and was already discussed above, the surface of the samples starts glowing after a specific period of time. However, for the mullite composition sample, the presence of molten sections is not visible as pronounced. Therefore, the higher temperature increase for the other aerogel samples might be caused by molten fractions on the surface still irradiating heat toward the sensor.

In addition to the phenomenological experiments in the arc-heated facility, thermal conductivity measurements have been conducted to justify and support the results mentioned above. In total, all materials have been analyzed to the maximum
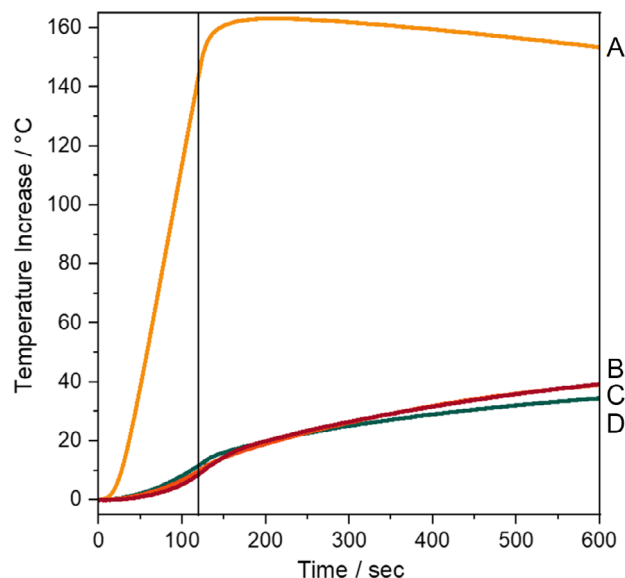

Figure 11. Diffraction pattern of the fiber-reinforced aerogel with desired mullite composition and mullite reference after a thermal treatment of 1,200 °C for 24 h.

Figure 12. Temperature increase measured behind the respective specimen a) glass fiber matt, b) silica aerogel fiber composite, c) opacified silica aerogel fiber composite, and d) mixed oxide aerogel fiber composite (mullite composition) over a period of 10 min (120 s arc-heated exposure).

**ADVANCED
SCIENCE NEWS**

www.advancedsciencenews.com

**ADVANCED
ENGINEERING
MATERIALS**

www.aem-journal.com

temperature applicable to the respective sample. The thermal conductivity of the pristine fiber mat sharply increases at elevated temperatures. The recorded values for the fiber mat do not match exactly with the ones provided by the supplier (cf. **Figure 13**). This fact might be attributed to different measuring conditions such as applied pressure. As the values are consistently higher than the theoretical ones a compression of the fibers could not be the explanation.

Figure 13 indicates that as expected all aerogel-containing composites outperform the fiber mat in terms of thermal conductivity in the lower temperature range.

Fitting the respective data shows that extrapolated thermal conductivities for the reinforced aerogel composite (B) would strongly increase which is attributable to the sintering effects already explained in the results above. Also, thermal conductivities could not be measured for higher temperatures due to degradation of the specimen. As expected, the opacified composites as well as the mixed oxide composites show a higher thermal conductivity.

In general, the opacified aerogel composite (C) exhibits a lower thermal conductivity than the mixed oxide composite (D) but a lower final application temperature. This is in accordance with the phenomenological results presented above since the mixed oxide also showed a faster temperature increase at the backside of the specimen (cf. Figure 12).

The thermal conductivity of the mixed oxide system exhibits lower values than the pristine fiber mat but initially higher values than the other aerogel composites which have been optimized in terms of thermal performances in previous studies.[21] However, these aerogel composites exhibit a steeper increase in thermal conductivity with application temperature as well as lower possible application temperature due to material failure in general compared to the new set of mixed oxide aerogel composites.

Based on the results presented above and the evaluation of the materials, it can be stated that the mixed oxide aerogels indeed exhibit the highest thermal stability and can withstand direct heat exposure without severe damage to the material. The thermal conductivity however is higher for the mixed oxide aerogels than for the opacified pure silica aerogels. This might be attributable to the fact that the skeleton itself has been changed from silica to a mixture of silica and alumina (or mullite). Both aluminum-containing oxides exhibit a higher thermal conductivity than pure silica. Pure bulk silica shows thermal conductivity values in the range of $1.5 \, \text{W} \, \text{m}^{-1} \, \text{K}^{-1}$,[41] whereas for alumina and mullite values of $14–18 \, \text{W} \, \text{m}^{-1} \text{K}^{-1}$ are reported.[42] This increase in thermal conductivity of the skeleton material might contribute to the explanation of why the mixed oxide aerogel exhibits higher thermal conductivities. In addition, no opacifier was used in the mixed oxide materials. Due to relatively long gelation times, a homogenous distribution of boehmite could not be guaranteed and was not considered although the performance of the opacified material was improved in comparison to the pure silica aerogel. The lack of boehmite opacifier inside the mixed oxide aerogel could also explain the slightly higher thermal conductivity. Missing an opacifier would reduce the absorption of IR radiation on the one hand. On the other hand, decomposition of the boehmite and release of water molecules could contribute to an overall lower thermal conductivity (see bubble formation in Figure S2, Supporting Information).

Additional gas sorption experiments reveal that the pore width distribution of the three different aerogel-containing samples differs. For pure silica aerogel an average pore width of $\approx22 \, \text{nm}$ can be found (see **Figure 14**). The other two aerogel-based materials
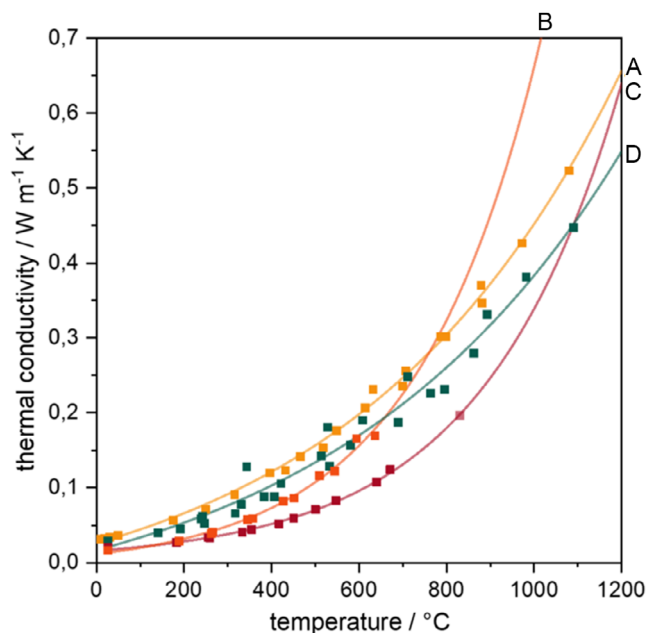
Figure 13. Temperature depending on thermal conductivity of a) glass fiber matt, b) silica aerogel fiber composite, c) opacified silica aerogel fiber composite, and d) mixed oxide aerogel fiber composite (mullite composition).
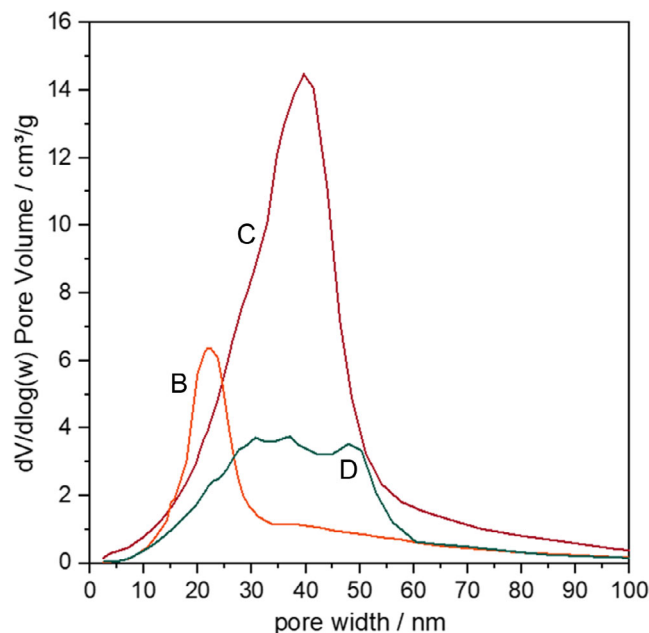
Figure 14. Pore width distribution of pure silica aerogel (B), opacified silica aerogel (C), and mixed oxide aerogel (D). [Note: (A) has intentionally been left out since it represents the pristine fiber mat throughout the manuscript.].

**ADVANCED
SCIENCE NEWS**

www.advancedsciencenews.com

**ADVANCED
ENGINEERING
MATERIALS**

www.aem-journal.com

exhibit slightly higher pore width. The opacified specimen shows an average pore width of ≈ 40 nm whereas for the aerogel in mullite composition, no distinct maximum can be measured. The pore width shows almost equally distributed values ranging from 30 to 50 nm. The total pore volume however is drastically decreased. The respective isotherms can be found in Figure S6, Supporting Information. BET analysis revealed specific surface areas of 273 m^2g^{-1} for pure silica aerogel, 187 m^2g^{-1} for the opacified material, and ≈ 242 m^2g^{-1} for the mixed oxide material.

These observations, especially the drastically decreased pore volume, in combination with the thermal conductivity of the skeleton might explain the different behavior in thermal conductivity. Although the overall performance of the mixed oxide material was superior in-depth investigation of the microstructure and the changes upon thermal treatment will be carried out and addressed in the future.

3. Conclusion

Within this study, we presented an optimization of an opacifier-free mixed oxide-based aerogel with fiber reinforcements for potential space ablator applications. The materials have been characterized in terms of thermal conductivity and thermal stability as well as producibility. Mixed metal oxide aerogel composites based on alumina and silica exhibit the best thermal stability for short-term application and do not show severe reconstructing and sintering effects after 120 s in an arc-heated facility. This thermal stability results in an increase in thermal conductivity. Therefore, the thermally most stable material does not exhibit the best insulating properties when compared to classical silica aerogels or opacified silica aerogels. Also, the thermal conductivity measurements revealed that shrinkage is observed for very long time periods. The experiments pointed out that despite being highly insulating the thermal stability is highly important so that the overall performance is improved although the thermal conductivity could be intrinsically higher. With this study, we point toward the high potential of aerogel composites as thermal ablator materials for space applications on the base of mixed metal oxides composites.

4. Experimental Section

Chemicals and Materials: Based on our recent publications,[21,43] ethanol (purity 99%) was used as solvent and was purchased from Chemsolute (Th. Geyer, Lohmar, Germany) and used in the syntheses without further purification. Tetraethyl orthosilicate (TEOS) was purchased from Merck (Darmstadt, Germany). Ammonium hydroxide solution (1 M) was purchased from Alfa Aesar (Thermo Fisher Scientific, Kandel, Germany). HCl (hydrochloric acid, 2 M) was purchased from Bernd Kraft (Duisburg, Germany). The opacifying boehmite particles were purchased from Nabaltec (Schwandorf, Germany), "Insulfrax LTX S Matte" insulating fiber mat was purchased from Insulcon GmBH (Neuss, Germany). Propylene oxide (PO) and aluminum chloride hexahydrate were purchased from Th. Geyer (Lohmar, Germany).

Manufacturing of Specimens: The syntheses for the fiber-reinforced silica aerogel as well as silica-boehmite system have been performed as described by Heyer et al.[21] For this demonstration, the following parameters have been chosen: For silica-based fiber reinforced aerogel a molar ration of TEOS:EtOH:H_2O HCl:NH_3 (1:8:6.4:2.3 $\times 10^{-4}$:2.3 $\times 10^{-2}$) was chosen [*whereas HCl was used as a 0.002 M aqueous solution*]. All precursors but ammonium hydroxide solution have been mixed and hydrolyzed at 50 °C under stirring for 45 min. Then, ammonium hydroxide solution was added to the solution which was then directly filled into the mold which already had the fiber mat inside.

For the synthesis of opacified silica-based fiber-reinforced aerogel a molar ration of TEOS:EtOH:H_2O:HCl:NH_3 was changed to (1:8:6.4:2,31 $\times 10^{-4}$: 2,31 $\times 10^{-2}$) [*whereas HCl was used as a 0.002 M aqueous solution*] to control the sedimentation of the opacifiers and the gelation time. The boehmite particles B30 (mass ratio TEOS:B30 was set to 5:1) was added after 40 min of stirring and 5 min before the ammonium hydroxide solution was added. For both approaches the specimens have been aged at 50 °C for 48 h.

Inspired by an original publication of Hurwitz et al.,[11a] mullite composition-based fiber-reinforced aerogel were synthesized using a molar ratios of TEOS:$AlCl_3 \times 6 \cdot H_2O$ (0.25:0.75), EtOH:H_2O has been set to (5:16) and $AlCl_3$: propylene oxide (PO) (1:3.75). In a typical synthesis, $AlCl_3 \times 6$ H_2O was added to water under stirring. Subsequently, TEOS and ethanol were added under stirring. The mixture was stirred for 90 min at 50 °C and then cooled to room temperature. The reaction container was sealed with a septum. PO [*pay attention to the toxicity of PO during handling!*] was added constantly with an air-sealed transfer system, then the mixture was stirred for 2 more minutes before it was filled in the respective container for molding. Gelation occurs typically within 30 min at room temperature. The samples had been aged for 24 h at room temperature and 7 d at 50 °C. All samples had been washed with ethanol to extract water and unreacted products. Subsequently dried in an extraction unit using supercritical CO_2 as extraction medium as already described previously in Heyer et al.[21]

Characterization: SEM images were recorded using a Zeiss Ultra 55. X-ray diffraction patterns were recorded using a Bruker D8 Advance diffractometer using CuK$_\alpha$, operating at 40 kV and 40 mA. CuK$_{\alpha 2}$ was subtracted mathematically from the patterns using Bruker Diffrac.EVA V5.2 software. Also, a background subtraction was performed to remove the exponential decay of the background of the pattern. Raman spectra were recorded using a Horiba XploRA plus Raman microscope equipped with a 10× magnification objective and a 532 nm laser. Gas sorption experiments were carried out using a Micromeritics 3Flex instrument. The analysis adsorptive was nitrogen operating at 77 K. All samples were preconditioned at 120 °C for 4 h under vacuum. Pore width distribution was obtained using the BJH method and specific surface areas were calculated using the BET method.

Test Facility: Thermal tests were performed in the L2K facility, which is one of the two test legs of DLR's arc-heated facilities LBK. The setup of LBK is schematically plotted in **Figure 15**. L2K uses a Huels-type arc heater with a maximum electrical power of 1.4 MW to energize the working gas to high enthalpy conditions. Hypersonic free stream velocities are provided by a convergent–divergent nozzle. The nozzle's expansion part is conical with a half angle of 12°. A more detailed description of the facility is given by Gülhan et al.[44] For the tests on aerogel samples, L2K was operated with air. The nozzle was set up with a 29 mm nozzle throat and a 200 mm wide exit.[45]
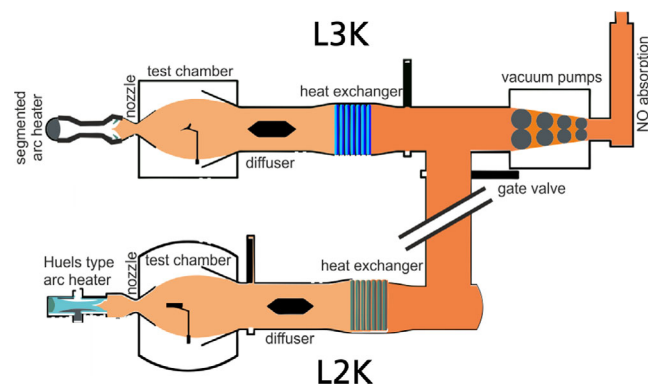

Figure 15. Sketch of the LBK facility.

The specimens were prepared as disks with a diameter of 100 mm. The front surface was exposed perpendicular to the flow (Figure 3). Test conditions and test position were chosen to apply a cold-wall heat flux of 230 kW m^{-2} to a fully catalytic material.

During facility start-up, the specimens were placed in the background of the L2K test chamber where they were affected by changing flow conditions inside the free stream. After the desired test conditions had been established, the specimen was moved into the flow and remained there for 120 s. Afterward, the specimen was moved out of the flow, before the arc heater was shut down.

At the test position, the front surface was monitored by an infrared camera AGEMA THV570, allowing measurement of the surface temperature distribution in a temperature range from 350 to 2,000 °C. In addition, the temperature on the backside of the specimens was measured by a type-K thermocouple.

The high-temperature thermal conductivities have been determined via the absolute plate method using the PMA4 device at TU Bergakademie Freiberg.

Supporting Information

Supporting Information is available from the Wiley Online Library or from the author.

Conflict of Interest

The authors declare no conflict of interest.

Data Availability Statement

Research data are not shared.

[1] N. Knoblauch, P. Mechnich, *Crystals* **2021**, *11*, 885.

[2] a) O. V. Basargin, T. M. Shcheglova, S. G. Kolyshev, V. Y. Nikitina, V. G. Maksimov, V. G. Babashov, *Glass Ceram.* **2013**, *70*, 43; b) C. Amaya, W. Aperador, J. C. Caicedo, F. J. Espinoza-Beltrán, J. Muñoz-Saldaña, G. Zambrano, P. Prieto, *Corros. Sci.* **2009**, *51*, 2994.

[3] a) İ. Şahin, Y. Özbakır, Z. İnönü, Z. Ulker, C. Erkey, *Gels*, **2018**, *4*, 3; b) A. Soleimani Dorcheh, M. H. Abbasi, *J. Mater. Process. Technol.* **2008**, *199*, 10.

[4] S. S. Kistler, *Nature* **1931**, *127*, 741.

[5] a) Z. Y. He, X. W. Zhang, W. Batchelor, *RSC Adv.* **2016**, *6*, 21435; b) J. Nemoto, T. Saito, A. Isogai, *ACS Appl. Mater. Interfaces* **2015**, *7*, 19809; c) Z. Pakowski, U. Nowacka, O. A. Zebida, M. Glebowski, *Inz. Chem. Procesowa* **2001**, *22*, 1085; d) Y. Xie, F. Guo, J. J. Mao, J. Y. Huang, Z. Chen, Y. X. Jiang, Y. K. Lai, *Sep. Purif. Technol.* **2021**, *254*, 117571; e) Z. H. Zeng, X. Y. D. Ma, Y. F. Zhang, Z. Wang, B. F. Ng, M. P. Wan, X. H. Lu, *ACS Sustainable Chem. Eng.* **2019**, *7*, 6959.

[6] a) P. Hao, Z. H. Zhao, J. Tian, H. D. Li, Y. H. Sang, G. W. Yu, H. Q. Cai, H. Liu, C. P. Wong, A. Umar, *Nanoscale* **2014**, *6*, 12120; b) G. J. He, M. Qiao, W. Y. Li, Y. Lu, T. T. Zhao, R. J. Zou, B. Li, J. A. Darr, J. Q. Hu, M. M. Titirici, I. P. Parkin, *Adv. Sci.* **2017**, *4*, 1600214; c) W. W. Liu, X. Li, M. H. Zhu, X. He, *J. Power Sources* **2015**, *282*, 179; d) J. J. Mao, J. Iocozzia, J. Y. Huang, K. Meng, Y. K. Lai, Z. Q. Lin, *Energy Environ. Sci.* **2018**, *11*, 772; e) W. Xia, C. Qu, Z. B. Liang, B. T. Zhao, S. G. Dai, B. Qiu, Y. Jiao, Q. B. Zhang, X. Y. Huang, W. H. Guo, D. Dang, R. Q. Zou, D. G. Xia, Q. Xu, M. L. Liu, *Nano Lett.* **2017**, *17*, 2788.

[7] K. W. Oh, D. K. Kim, S. H. Kim, *Fibers Polym.* **2009**, *10*, 731.

[8] a) T. Woignier, G. W. Scherer, A. Alaoui, *J. Sol-Gel Sci. Technol.* **1994**, *3*, 141; b) T. Woignier, J. Phalippou, F. Despetis, S. Calas-Etienne, in *Handbook of Sol-Gel Science and Technology* (Eds: L. Klein, M. Aparicio, A. Jitianu), Springer, Cham Switzerland **2018**, https://doi.org/10.1007/978-3-319-32101-1_27; c) T. Woignier, J. Phalippou, H. Hdach, G. W. Scherer, *presented at Symp. on Better Ceramics through Chemistry 4*, San Francisco, CA, April **1990**; d) N. Husing, U. Schubert, *Angew. Chem. Int. Ed.* **1998**, *37*, 23; e) M. Koebel, A. Rigacci, P. Achard, *J. Sol-Gel Sci. Technol.* **2012**, *63*, 315; f) E. Strobach, B. Bhatia, S. Yang, L. Zhao, E. N. Wang, *APL Mater.* **2019**, *7*, 081104.

[9] a) W. Dang, B. W. Wang, Z. L. Xu, X. Y. Zhang, F. P. Li, K. Zhao, X. Hu, Y. F. Tang, *J. Non-Cryst. Solids* **2023**, *600*, 122031; b) A. S. Shalygin, A. A. Katcin, A. Y. Barnyakov, A. F. Danilyuk, O. N. Martyanov, *Ceram. Int.* **2021**, *47*, 9585; c) X. Q. Wang, C. Y. Li, *Indian J. Chem. Technol.* **2023**, *30*, 198.

[10] a) A. Rose, A. Hofmann, P. Voepel, B. Milow, R. Marschall, *ACS Appl. Energy Mater.* **2022**, *5*, 14966; b) T. T. Niu, B. Zhou, Z. H. Zhang, J. M. Yang, X. J. Ji, J. Shen, Z. H. Zhang, A. Du, *Front. Mater.* **2021**, *8*, 674578.

[11] a) F. I. Hurwitz, M. Gallagher, T. C. Olin, M. K. Shave, M. A. Ittes, K. N. Olafson, M. G. Fields, R. B. Rogers, H. Q. Guo, *Int. J. Appl. Glass Sci.* **2014**, *5*, 276; b) Y. Mizushima, M. Hori, *J. Mater. Res.* **1993**, *8*, 2993.

[12] a) P. L. Hu, Y. J. Sun, B. Z. Gao, M. Gong, B. Luo, J. P. Fan, *Ceram. Int.* **2022**, *48*, 18699; b) N. S. Olson, F. I. Hurwitz, H. Q. Guo, N. J. Madden, J. L. Stokes, R. B. Rogers, J. A. Krogstad, *J. Am. Ceram. Soc.* **2021**, *104*, 4190.

[13] F. Rechberger, F. J. Heiligtag, M. J. Suess, M. Niederberger, *Angew. Chem. Int. Ed.* **2014**, *53*, 6823.

[14] a) H. Schafer, B. Milow, L. Ratke, *RSC Adv.* **2013**, *3*, 15263; b) C. N. Chervin, B. J. Clapsaddle, H. W. Chiu, A. E. Gash, J. H. Satcher, S. M. Kauzlarich, *Chem. Mater.* **2005**, *17*, 3345; c) X. Li, G. T. Qin, Y. T. Wang, W. Wei, *J. Porous Mater.* **2014**, *21*, 611; d) A. Feinle, N. Husing, *J. Supercrit. Fluids* **2015**, *106*, 2; e) Y. Mizushima, M. Hori, *J. Mater. Res.* **1994**, *9*, 2272; f) J. F. Poco, J. H. Satcher, L. W. Hrubesh, *J. Non-Cryst. Solids* **2001**, *285*, 57; g) G. Q. Zu, J. Shen, W. Q. Wang, L. P. Zou, Y. Lian, Z. H. Zhang, B. Liu, F. Zhang, *Chem. Mater.* **2014**, *26*, 5761; h) X. D. He, H. X. Zhang, Y. L. Hong, C. Q. Hong, in *Nanoscience and*

Technology, Pts 1 and 2 (Eds: C. Bai, S. Xie, X. Zhu), Vols. *121–123*, Trans Tech Publications Ltd, Durnten-Zurich **2007**; i) J. F. Yang, Q. H. Wang, T. M. Wang, *J. Sol-Gel Sci. Technol.* **2017**, *83*, 527.

[15] E. P. Office, https://cordis.europa.eu/programme/id/HORIZON.2.4 (accessed: February 2023).

[16] F. Gomollón-Bel, *Chem. Int.* **2022**, *44*, 4

[17] a) G. Q. Zu, J. Shen, L. P. Zou, W. Q. Wang, Y. Lian, Z. H. Zhang, A. Du, *Chem. Mater.* **2013**, *25*, 4757; b) B. E. Yoldas, *J. Mater. Sci.* **1975**, *10*, 1856; c) T. Horiuchi, T. Osaki, T. Sugiyama, H. Masuda, M. Horio, K. Suzuki, T. Mori, T. Sago, *J. Chem. Soc. Faraday Trans.* **1994**, *90*, 2573.

[18] H. Gao, Z. Zhang, Z. Shi, J. Zhang, M. Zhi, Z. Hong, *J. Sol-Gel Sci. Technol.* **2018**, *85*, 567.

[19] a) T. Horiuchi, L. Chen, T. Osaki, T. Sugiyama, K. Suzuki, T. Mori, *Catal. Lett.* **1999**, *58*, 89; b) T. Horiuchi, T. Osaki, T. Sugiyama, K. Suzuki, T. Mori, *J. Non-Cryst. Solids* **2001**, *291*, 187.

[20] H.-N.-R. Jung, V. G. Parale, T. Kim, H. H. Cho, H.-H. Park, *Ceram. Int.* **2018**, *44*, 10579.

[21] M. Heyer, A. Berkefeld, P. Voepel, B. Milow, *Materials* **2020**, *13*, 2677.

[22] T. A. Heppenheimer, *Facing the Heat Barrier: A History of Hypersonics* The NASA History Series, National Aeronautics and Space Administration, Washington, DC **2007**

[23] O. Uyanna, H. Najafi, *Acta Astronaut.* **2020**, *176*, 341.

[24] B. Helber, A. Turchi, J. B. Scoggins, A. Hubin, T. E. Magin, *Int. J. Heat Mass Transfer* **2016**, *100*, 810.

[25] a) K. Triantou, B. Perez, A. Marinou, S. Florez, K. Mergia, G. Vekinis, J. Barcena, W. Rotarmel, C. Zuber, A. de Montbrun, *Compos. Part B* **2017**, *108*, 270; b) L. A. Pillai, N. Sreenivas, K. Krishnaraj, V. Unnikrishnan, M. Ajith, *J. Heat Transfer Trans. ASME* **2018**, *140*, 072801; c) G. Pelin, C. E. Pelin, A. Ştefan, I. Dincă, E. Andronescu, O. Oprea, D. Ficai, R. Truşcă, *Bull. Mater. Sci.* **2018**, *41*, 28.

[26] a) J. Lachaud, I. Cozmuta, N. N. Mansour, *J. Spacecraft Rockets* **2010**, *47*, 910; b) A. Huang, https://www.nasa.gov/centers/ames/thermal-protection-materials/tps-materials-development/low-density-ablators.html (accessed: May 2023).

[27] P. N. Desai, R. A. Mitcheltree, F. M. Cheatwood, *J. Spacecraft Rockets* **1999**, *36*, 463.

[28] R. D. Launius, D. R. Jenkins, NASA **2012**.

[29] R. Hoover, https://www.nasa.gov/exploration/commercial/cargo/spacex_heatshield.html (accessed: May 2023).

[30] a) R. J. Black, J. M. Costa, B. Moslehi, L. Zarnescu, D. Hackney, K. Peters, *Proc. SPIE 9062*, Vol. *9062*, Smart Sensor Phenomena, Technology, Networks, and Systems Integration, San Diego, California, United States 10 April **2014**, p. 906204; b) M. J. Wright, R. A. S. Beck, K. T. Edquist, D. Driver, S. A. Sepka, E. M. Slimko, W. H. Willcockson, *J. Spacecraft Rockets* **2014**, *51*, 1125.

[31] a) H. Smith, https://www.nasa.gov/directorates/spacetech/game_changing_development/projects/MEDLI-2 (accessed: September 2023); b) K. T. Edquist, B. R. Hollis, A. A. Dyakonov, B. Laub, M. J. Wright, T. P. Rivellini, E. M. Slimko, W. H. Willcockson, *presented at 2007 IEEE Aerospace Conf.*, Big Sky, MT, March **2007**.

[32] Y.-Z. Ma, H.-S. Li, Z.-Z. Zhao, *Struct. Multidiscip. Optim.* **2021**, *64*, 1199.

[33] L. Ferrari, M. Barbato, B. Esser, I. Petkov, M. Kuhn, S. Gianella, J. Barcena, C. Jimenez, D. Francesconi, V. Liedtke, A. Ortona, *Compos. Struct.* **2016**, *154*, 61.

[34] a) T. Hermann, H. Ifti, M. McGilvray, L. Doherty, R. Geraets, In *HiSST: Int. Conf. on High-Speed Vehicle Science Technology*, Moscow November **2018**; b) M. Wall, https://www.space.com/43101-elon-musk-explains-stainless-steel-starship.html (accessed: August 2023).

[35] Insulfrax LTX-Matte | Products | Unifrax, https://www.unifrax.com/de/product/insulfrax-ltx-blanket/ (accessed: February 2023).

[36] a) I. H. Jung, S. A. Decterov, A. D. Pelton, *J. Eur. Ceram. Soc.* **2005**, *25*, 313; b) W. Huang, M. Hillert, X. Wang, *Metall. Mater. Trans. A* **1995**, *26*, 2293.

[37] F. J. Klug, S. Prochazka, R. H. Doremus, *J. Am. Ceram. Soc.* **1987**, *70*, 750.

[38] G. Eriksson, A. D. Pelton, *Metall. Trans. B* **1993**, *24*, 807.

[39] a) L. B. Kong, Y. B. Gan, J. Ma, T. S. Zhang, F. Boey, R. F. Zhang, *J. Alloys Compd.* **2003**, *351*, 264; b) A. N. Abramov, A. D. Plekhovich, A. M. Kut'in, M. V. Yashkov, A. N. Guryanov, *Inorg. Mater.* **2018**, *54*, 940.

[40] B. Lafuente, R. T. Downs, H. Yang, N. Stone, in *Highlights in Mineralogical Crystallography* (Eds: T. Armbruster, R. M. Danisi), De Gruyter (O), Berlin, München, Boston **2015**.

[41] W. Zhu, G. Zheng, S. Cao, H. He, *Sci. Rep.* **2018**, *8*, 10537.

[42] Y. Hirata, T. Shimonosono, *J. Korean Ceram. Soc.* **2016**, *53*, 43.

[43] A. Berkefeld, M. Heyer, B. Milow, *J. Sol-Gel Sci. Technol.* **2017**, *84*, 486.

[44] a) B. Esser, A. Guelhan, in *5th European Workshop on Thermal Protection Systems and Hot Structures*, Noordwijk, The Netherlands 17–19 May **2006**; b) A. Guelhan, B. Esser, U. Koch, *AIAA J. Spacecraft Rockets* **2001**, *38*, 199.

[45] D. J. Duval, S. H. Risbud, J. F. Shackelford, *Ceramic and Glass Materials* (Eds: J. F. Shackelford, R. H. Doremus), Springer, Boston, MA **2008**, p. 27.